A PROPELLER SLIPSTREAM MODEL IN SUBSONIC LINEARIZED POTENTIAL FLOW

Per Lötstedt
SAAB Aircraft Division, SAAB-SCANIA, S-581 88 Linköping, Sweden

Abstract

A model for computation of the time-averaged subsonic flow field over a nacelle and a wing induced by a propeller has been developed. The slipstream model is based on classical propeller theory and is included in an existing panel program. The geometry of the slipstream is determined by the nacelle. The influence of the propeller is given by a combined momentum-blade element theory. No experimental data are necessary. The computed pressures and velocities are compared to windtunnel data for two angles of attack and two geometries: an axisymmetric nacelle and a wing and a non-axisymmetric nacelle and a wing.

1 Introduction.

The prediction of the influence of the propeller slipstream on the flow is important in the design phase of a new propeller driven aircraft. The flow pattern over the nacelle and the wing is affected considerably by a tractor propeller mounted on the wing in particular at take-off conditions. Panel methods are a standard tool for aerodynamical computations around three-dimensional configurations at subsonic speeds, see e. g. [11]. Usually panel programs are written to solve potential flow problems, but they can be amended to handle also the vortical flow behind a rotating propeller. The advantage of panel methods is that they are easy to use and inexpensive in terms of CPU time. When a propeller slipstream capability is added to a panel program the extension should also have these two properties. The flow in the slipstream is much more complicated than ordinary freestream flow and simplifications in the computational model are necessary. Thus, we cannot expect to obtain the same accuracy in the predictions with the slipstream as we are used to without the slipstream. This is true also for windtunnel experiments.

In this paper we describe a propeller slipstream model which has been incorporated in an existing panel program [14]. The time-averaged flow behind the propeller is generated by a system of vortices following classical propeller theory [16]. The strength of the vortices is determined by a combined momentum-blade element theory. The propeller data needed in the simulation are the number of blades, the geometry of the blades, the speed of revolution etc. No supporting windtunnel experiment is necessary. The geometry of the slipstream is approximated taking the surface of the nacelle into account. This is important in order to obtain realistic pressures on the nacelle. The velocities in the slipstream determined by the model are introduced together with the freestream as onset flow in the panel method. The variation of the total pressure inside the slipstream is given by one of two implemented options based on momentum theory.

The computed pressures and velocities are compared to windtunnel measurements from FFA [21],[22]. The configuration geometries are an axisymmetric nacelle with a wing [22] and a non-axisymmetric nacelle with a wing [21]. The non-axisymmetric nacelle is such that the shape of the innermost sections of the slipstream is changed by the presence of the nacelle. The Mach number is 0.15 and the angle of attack α is 0° or 5°. The chosen propeller data correspond to a take-off case with a contribution from the slipstream in the freestream direction of more than 60 % of the freestream speed. The c_p values on the wing and nacelle and the velocities in the slipstream outside the nacelle are compared. The agreement in the simplest case, the axisymmetric nacelle at $\alpha = 0°$, is quite good. In the more complex flows around the non-axisymmetric nacelle the influence of the slipstream on the wing pressures is overestimated in comparison with the experiments.

The time-averaged flow over a nacelle and a wing behind a propeller has been computed previously using panel methods, nonlinear potential equations and the Euler equations. In [1],[2],[8],[9],[12], [23] a panel method is the basis for the development of the slipstream model. The slipstream is modeled analytically in [1],[2] and [12]. The configuration in these papers is a nacelle with a wing. The computed pressures in [2] are compared to experimental data at the wing. A propeller panel model is presented in [9]. The model is applied in [23] to a complete aircraft configuration with aft-mounted pusher propellers and the computations are compared to windtunnel results. In [8] the same model is developed to predict the flow over a nacelle and wing behind a tractor propeller. Propeller simulation codes for higher Mach numbers must be based on solvers of nonlinear equations. In [5] a program for solution of the transonic small perturbation equation is extended to include slipstream effects. The computed pressures are compared to experiments for a swept wing and a nacelle. The full potential equation is used in [18] and [20]. The configuration in [18] is a wing and in [20] a nacelle and a wing. Comparisons are made with measurements over the wing in both papers. The slipstream effects are modeled analytically using windtunnel data in [5], [18] and [20]. The Euler equations and a slipstream defined by experiments are solved over a wing in [24] and a nacelle-wing combination in [3] and [19]. The calculated pressures are compared to experimental results on the wing.

In all the references above the nacelle section is fairly small in comparison to the propeller disc and there is no experimental validation of the computed nacelle pressures. Many of the methods are not satisfactory if the nacelle modifies the slipstream geometry considerably behind the propeller. In most cases the calculations rely on experimental data or analytical approximations of the slipstream

properties. No velocities in the flow field are compared to measurements but only c_p values on the wing surfaces.

The rest of the paper is organized as follows. In the next section the physical and mathematical background for the slipstream model is given. Then the computational method is described in section 3. The geometry of the slipstream is determined in the first step. In the second step the singularity distribution in the slipstream is computed, the onset flow at the solid surfaces of the configuration is calculated and then the panel method is invoked to obtain the complete flow field. Comparisons with windtunnel experiments are made in section 4. The conclusions are drawn in the final section.

The author has had many fruitful discussions with Bert Arlinger on the subject of this paper.

2 Background in physics and mathematics.

This section is divided into two parts. We begin by deriving the basic relations for the representation of the vortical flow inside the slipstream. Then the blade element theory and the coupling to the slipstream model are reviewed.

2.1 The slipstream model.

If we are interested in the time-average of the influence of the propeller on the downstream nacelle and wing surfaces, then the classical model replaces the discrete propeller blades by a continuum of propellers on a disk [10]. Therefore, the slipstream consists of a continuum of propeller wakes and the velocity is a smooth time-independent variable.

Let $\mathbf{v}$ be the velocity of the flow

$$\mathbf{v} = (v_x, v_y, v_z)^T,$$

Φ a scalar potential and $\mathbf{A}$ a vector potential. In incompressible flow it follows from the continuity equation that $\mathbf{v}$ is divergence free

$$\nabla \cdot \mathbf{v} = 0. \tag{1}$$

By Helmholtz's decomposition theorem $\mathbf{v}$ can be split into two parts $\mathbf{v_1}$ and $\mathbf{v_2}$ with the properties

$$\begin{aligned} &\mathbf{v} = \mathbf{v_1} + \mathbf{v_2}, \\ &\mathbf{v_1} = \nabla \times \mathbf{A}, \quad \nabla \cdot \mathbf{v_1} = 0, \\ &\mathbf{v_2} = \nabla \Phi, \qquad \nabla \times \mathbf{v_2} = 0. \end{aligned} \tag{2}$$

The rotational part of the flow in the slipstream is represented by $\mathbf{v_1}$ and $\mathbf{A}$ and the irrotational part, e. g. in the freestream, is represented by $\mathbf{v_2}$ and Φ. The potential Φ consists of two terms: the freestream potential Φ_∞ and the potential due to the submerged body in the flow Φ_i,

$$\Phi = \Phi_\infty + \Phi_i. \tag{3}$$

It follows from (1) and (2) that

$$\nabla \cdot \mathbf{v} = \nabla \cdot \mathbf{v_2} = \Delta \Phi = 0. \tag{4}$$

The equation (4) is solved for Φ by the panel method in [11]. The method is of the same type as e. g. VSAERO [15] and PANAIR [6]. The boundary condition on Φ is a Dirichlet condition at the inner boundary of the configuration. This condition is usually chosen to be Φ_∞. Let (ξ, η, ζ) be a point on the configuration surface C and (x, y, z) an arbitrary point in space. Define

$$\mathbf{r} = (x - \xi, y - \eta, z - \zeta)^T,$$

$$r = |\mathbf{r}| = \sqrt{(x-\xi)^2 + (y-\eta)^2 + (z-\zeta)^2},$$

and introduce the notation

$$\mathbf{b} = \nabla_\xi (1/r) = -\nabla_x (1/r) = \mathbf{r}/r^3.$$

The differentiation in the operator ∇ is made with respect to the (x, y, z) or the (ξ, η, ζ) variables depending on the index. In the panel method [14] Φ_i in (3) is written as an integral over C of the surface singularity distributions $\mu_C(\xi, \eta, \zeta)$ (doublets) and $\sigma_C(\xi, \eta, \zeta)$ (sources and sinks)

$$\Phi_i(x, y, z) = \frac{1}{4\pi} \int_C (\mu_C \mathbf{n} \cdot \mathbf{b} - \sigma/r)\, dC. \tag{5}$$

The boundary condition on the velocity $\mathbf{v}$ at the solid surfaces is

$$\mathbf{v} \cdot \mathbf{n} = \mathbf{v_1} \cdot \mathbf{n} + \mathbf{v_2} \cdot \mathbf{n} = 0, \tag{6}$$

where $\mathbf{n}$ is the normal of the surface. In (5) σ_C is equal to the jump in $\mathbf{v} \cdot \mathbf{n}$ at C. In the interior of C the velocity is

$$\mathbf{v_1} + \nabla \Phi_\infty = \mathbf{v_1} + \mathbf{v_{2\infty}}.$$

Thus, by (6)

$$\sigma_C = -(\mathbf{v_1} + \mathbf{v_{2\infty}}) \cdot \mathbf{n}. \tag{7}$$

The doublet distribution μ_C in (5) is determined such that Φ_i satisfies the Dirichlet condition

$$\Phi_i = 0 \tag{8}$$

in the interior of C.

The representation of the irrotational part of the flow is described above. We now turn to the vortical flow generated by the propeller. Let (ξ, η, ζ) be a point in the slipstream Ω behind the propeller. Introduce a volume doublet singularity distribution $\vec{\mu}(\xi, \eta, \zeta) \in \mathcal{R}^3$ in Ω and define $\mathbf{A}$ to be

$$\mathbf{A} = \frac{1}{4\pi} \int_\Omega \vec{\mu} \times \mathbf{b}\, d\Omega. \tag{9}$$

Insert the identity

$$\nabla_\xi \times (\vec{\mu}/r) = \nabla_\xi \times \vec{\mu}/r + \mathbf{b} \times \vec{\mu},$$

into (9) and integrate by parts applying the following generalization of Gauss' theorem for an arbitrary vector $\mathbf{a}$

$$\int_\Omega \nabla_\xi \times \mathbf{a}\, d\Omega = \int_S \mathbf{n} \times \mathbf{a}\, dS$$

to obtain

$$\begin{aligned} \mathbf{A} &= \frac{1}{4\pi} \int_\Omega (\nabla_\xi \times \vec{\mu}/r - \nabla_\xi \times (\vec{\mu}/r))\, d\Omega = \\ &= \frac{1}{4\pi} \int_\Omega \nabla_\xi \times \vec{\mu}/r\, d\Omega - \frac{1}{4\pi} \int_S \mathbf{n} \times \vec{\mu}/r\, dS, \end{aligned} \tag{10}$$

where S is the surface of Ω and $\mathbf{n}$ is its normal. With the volume and surface vorticity, $\mathbf{\Gamma}$ and $\mathbf{\Gamma}_S$,

$$\mathbf{\Gamma} = \nabla_\xi \times \vec{\mu}, \ \mathbf{\Gamma}_S = \mathbf{n} \times \vec{\mu}, \tag{11}$$

the vector potential $\mathbf{A}$ in (10) can be written

$$\mathbf{A} = \frac{1}{4\pi}\int_\Omega \mathbf{\Gamma}/r \, d\Omega - \frac{1}{4\pi}\int_S \mathbf{\Gamma}_S/r \, dS, \tag{12}$$

By (12) the rotational part of $\mathbf{v}$ is

$$\mathbf{v}_1 = \nabla_x \times \mathbf{A} =$$

$$= \frac{1}{4\pi}\int_\Omega \nabla_x \times (\mathbf{\Gamma}/r) \, d\Omega - \frac{1}{4\pi}\int_S \nabla_x \times (\mathbf{\Gamma}_S/r) \, dS. \tag{13}$$

Introduce the relations

$$\nabla_x \times (\mathbf{\Gamma}/r) = \nabla_x \times \mathbf{\Gamma}/r + \nabla_x(1/r) \times \mathbf{\Gamma} = -\mathbf{b} \times \mathbf{\Gamma},$$

$$\nabla_x \times (\mathbf{\Gamma}_S/r) = \mathbf{\Gamma}_S \times \mathbf{b},$$

into (13) and we have derived the Biot-Savart law

$$\mathbf{v}_1 = \frac{1}{4\pi}\int_\Omega \mathbf{\Gamma} \times \mathbf{b} \, d\Omega - \frac{1}{4\pi}\int_S \mathbf{\Gamma}_S \times \mathbf{b} \, dS. \tag{14}$$

The vector potential $\mathbf{A}$ is solenoidal since

$$\nabla_x \cdot \mathbf{A} = \frac{1}{4\pi}\int_\Omega (\mathbf{b} \cdot \nabla_x \times \vec{\mu} - \vec{\mu} \cdot \nabla_x \times \mathbf{b}) \, d\Omega = 0.$$

One can show that

$$\nabla_x \times \mathbf{v} = \nabla_x \times \mathbf{v}_1 = \nabla_x \times \vec{\mu}(x, y, z) = \mathbf{\Gamma}, \tag{15}$$

thus confirming the interpretation of $\mathbf{\Gamma}$ in (11) as a vorticity distribution.

We have found that the rotational flow with velocity $\mathbf{v}_1$ can be written as the curl of a vector potential $\mathbf{A}$. This potential $\mathbf{A}$ can be represented by a doublet density $\vec{\mu}$ in the volume Ω occupied by the slipstream where $\vec{\mu} \neq 0$ and $\nabla \times \mathbf{v}_1 \neq 0$, cf. (9), (10) and (15). An alternative is to introduce a vorticity distribution $\mathbf{\Gamma}$ in Ω and $\mathbf{\Gamma}_S$ on S as in (14). The relation between $\mathbf{\Gamma}$, $\mathbf{\Gamma}_S$ and $\vec{\mu}$ is given by (11).

The influence of $\mathbf{A}$ outside Ω is small such that $\mathbf{v}_1$ vanishes rapidly in $\mathcal{R}^3 \setminus \Omega$. Moreover, we know from the theory of panel methods that

$$\lim_{r\to\infty} \nabla\Phi_i = 0.$$

Thus, the correct boundary condition at ∞

$$\mathbf{v} = \nabla\Phi_\infty = \mathbf{v}_{2\infty}$$

outside Ω is satisfied. The boundary condition at the solid surfaces (6) is also fulfilled. The total velocity $\mathbf{v}$ is divergence free (1). We have a solution $\mathbf{v}$ that solves our problem.

The outline of the computational method is as follows:

- Determine $\vec{\mu}$ in the slipstream Ω or $\mathbf{\Gamma}$ in Ω and $\mathbf{\Gamma}_S$ on S by the combined momentum-blade element theory described in the next subsection.
- Compute the rotational part $\mathbf{v}_1$ of the flow by (14) and (11).
- Insert $\mathbf{v}_1$ and the freestream speed $\mathbf{v}_{2\infty}$ into (7). Then solve the integral equation defined by (8) and (5) for the doublet surface distribution μ_C.
- Compute Φ in (3) and its gradient and use (2) to obtain the total velocity $\mathbf{v}$. By Bernoulli's equation and the jump in the total pressure at the propeller disk c_p can be calculated inside and outside the slipstream Ω.

2.2 The momentum-blade element theory.

The combined momentum and simple blade element theory employed to determine the vorticity in the slipstream is described briefly. For a detailed account see [10],[13] and [16].

Let the x axis in a cylindrical coordinate system coincide with the propeller axis and let the θ coordinate define the azimuthal position. The distance from the propeller axis is r. The components of $\mathbf{v}$ are

$$\mathbf{v} = (v_x, v_\theta, v_r)^T.$$

The notation in this subsection is as follows. The total thrust of the propeller is T and dT is the thrust of an annulus of the propeller disk. The density of the air is ρ, the number of blades is n_b and the speed of rotation at r is ωr. The two-dimensional propeller section has the angle β between the disk and the zero lift line and the unknown induced angle of attack is α_i as illustrated in fig. 1. If the freestream flow is parallel to the propeller axis then the vorticity Γ shed by the continuum of propellers is constant in the azimuthal direction θ. With $\alpha \neq 0°$ Γ is a function of both r and θ.

Let $2w$ be the increase in the axial velocity far downstream in the slipstream at distance r from the propeller axis. Assume that the freestream is parallel to the axis. Then the momentum theory and the definitions of V_R and ϕ in fig. 1 give the thrust from the annulus at r of width dr

$$dT = \rho(2\pi r \, dr)(v_{2\infty} + w)2w =$$

$$= \rho(2\pi r \, dr)(v_{2\infty} + \alpha_i V_R \cos\phi)2\alpha_i V_R \cos\phi, \tag{16}$$

where

$$v_{2\infty} = |\mathbf{v}_{2\infty}|,$$

$$V_R = \sqrt{v_{2\infty}^2 + (\omega r)^2}.$$

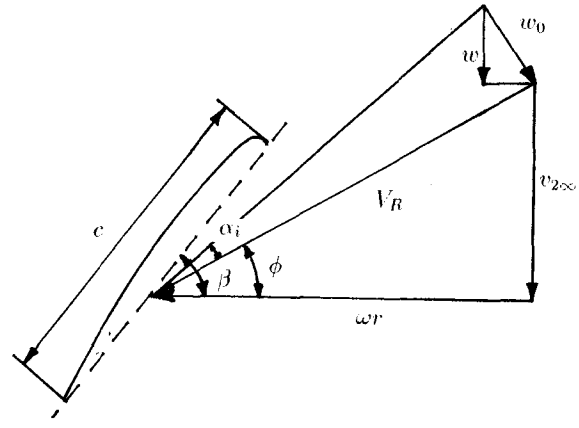

Figure 1: The angles and velocities at a propeller blade.

Let a_0 be defined by the sectional lift coefficient c_l and

$$c_l = a_0(\beta - \phi - \alpha_i). \tag{17}$$

Then by blade element theory the lift dL of a propeller blade section with chord c is

$$dL = \frac{1}{2}\rho V_R^2 c a_0(\beta - \phi - \alpha_i), \tag{18}$$

and the thrust from n_b blades is

$$dT = n_b dL \cos\phi. \tag{19}$$

Let dT in (16) and (19) be equal and solve the resulting equation for α_i.

Assume that the strength of the vortex filament leaving the trailing edge of the blade section is Γ and that the angle between the disk and the filament is ψ

$$\psi = \phi + \alpha_i. \tag{20}$$

The total vorticity $d\Gamma$ shed from the trailing edges of the blades at r is given by the Kutta-Joukowski theorem in two dimensions

$$d\Gamma = dL/(\rho V_R), \tag{21}$$

and the vortex strength is

$$\Gamma = d\Gamma/(2\pi r\, dr). \tag{22}$$

This Γ is transformed further in section 3 to fit the requirements of the vorticity distribution in (14) for computation of $\mathbf{v}_1$.

If more accurate data on c_l of the blade sections are available then the simple formula (17) for c_l can be replaced in (18). A correction of c_l is always introduced based on the local Mach number, cf. [13]. The blade element approximation above is truly two-dimensional and three-dimensional effects are not modeled. As a remedy the lift in the tip region is modified smoothly such that $c_l = 0$ at the tip, cf. [13].

2.3 The pressure jump.

According to incompressible propeller theory the axial speed is continuous but the static pressure is discontinuous when the flow passes the propeller disk, see [16]. Two different ways of obtaining the size of the pressure jump will be presented in the case when the freestream is parallel to the propeller axis.

In the first alternative the pressure discontinuity Δp is derived from the theory in the previous subsection. At a distance r from the propeller axis Δp is

$$\Delta p = dT/(2\pi r\, dr), \tag{23}$$

where the thrust is

$$dT = \frac{1}{2} n_b \rho V_R^2 c(c_l \cos\phi - c_d \sin\phi) dr.$$

The sectional drag coefficient is here c_d. Using (23) the c_p coefficient is modified by a constant value Δc_p in each streamtube starting at the propeller disk. This value is determined at the disk to be

$$\Delta c_p = \Delta p/(\frac{1}{2}\rho v_{2\infty}^2). \tag{24}$$

Far downstream in the fully contracted slipstream the static pressure is equal to the freestream static pressure p_∞, see [16]. The second alternative is derived from this fact. The velocity in the slipstream far downstream is denoted by $\mathbf{v}_*$. Neglecting v_r it follows from Bernoulli's equation that

$$p_\infty + \frac{1}{2}\rho(v_{*x}^2 + v_{*\theta}^2) = p + \frac{1}{2}\rho(v_x^2 + v_\theta^2) \tag{25}$$

in the slipstream. The pressure coefficient is by (25)

$$c_p = (p - p_\infty)/(\frac{1}{2}\rho v_{2\infty}^2) = (v_{*x}^2 + v_{*\theta}^2 - (v_x^2 + v_\theta^2))/v_{2\infty}^2. \tag{26}$$

Introduce

$$v_{*x} = v_{2\infty} + 2w$$

into (26) to obtain

$$\begin{aligned} c_p &= (v_{2\infty}^2 - (v_x^2 + v_\theta^2))/v_{2\infty}^2 + \\ &\quad +((2w)^2 + 4v_{2\infty}w + v_{*\theta}^2)/v_{2\infty}^2 = \\ &= c_{p0} + (2 + (2w/v_{2\infty}))(2w/v_{2\infty}) + (v_{*\theta}/v_{2\infty})^2. \end{aligned} \tag{27}$$

The usual pressure coefficient is c_{p0} in (27) and the last two terms correspond to Δc_p in (24). The formula for the static pressure used in [12] is (27).

From the Euler equations it follows that there is a pressure gradient in the radial direction in a stationary rotating flow field

$$\frac{dp}{dr} = \frac{\rho v_\theta^2}{r}. \tag{28}$$

By the definition of c_p and (28) we have

$$\frac{dc_p}{dr} = \frac{2}{r}\left(\frac{v_\theta}{v_{2\infty}}\right)^2 \geq 0. \tag{29}$$

The equation (29) can be integrated in the radial direction in the far downstream slipstream from the outer boundary into the interior to obtain the variation $\delta c_p(r)$ of c_p due to the rotation. The theory leading to (26) and (27) does not include this effect. Hence, by adding $\delta c_p(r)$ to c_p in (27) the right behavior of p in the fully contracted slipstream is achieved. This term is usually small.

3 Computational model.

The solution process is split into two separate steps which are independent of each other. First, the outer boundary and the inner structure of the slipstream is generated by following streamlines starting at the propeller disk. These streamlines are computed by the panel method [14]. In the second step the flow field about the configuration is determined following the outline at the end of section 2.1.

The coordinate system in this section is the same cylindrical system as in section 2.2. The propeller axis is a part of the x axis and freestream flow perpendicular to the propeller disk has $\alpha = 0°$.

3.1 The slipstream discretization.

The slipstream Ω is divided into a number of non-overlapping cells ("field panels") ω_{ijk}, $i = 1, \ldots, l$, $j = 1, \ldots, m$, $k = 1, \ldots, n$, see fig. 2. The index i runs in the x direc-

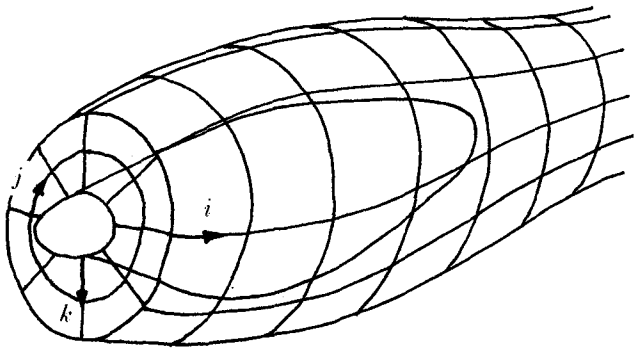

Figure 2: The discretization of the slipstream around a nacelle. In this case $l > 6$, $m = 8$ and $n = 2$.

tion, j in the θ direction and k in the r direction. The slipstream is unbounded in the positive x direction, but in the computations we extend the slipstream to $x = x_{end}$ only, such that l and the volume of each ω_{ijk} are finite. If x_{end} is chosen sufficiently far downstream then the influence of this limit is small on the flow in the neighborhood of the configuration. Then Ω can be written

$$\Omega = \bigcup_{\substack{i=1,l \\ j=1,m \\ k=1,n}} \omega_{ijk}.$$

The cells ω_{ijk} are distorted cubes defined by their 8 corners, see fig. 3. There is a doublet density $\vec{\mu}_{ijk}$ associated with each ω_{ijk}.

In order to compute $\vec{\mu}_{ijk}$ a number of simplifications are introduced. A vortex tube is defined by a number of vortex filaments in the same way as streamlines define a stream tube. According to the first vortex theorem [4] the circulation around a vortex tube is constant along the tube. If B is an arbitrary cross section of the tube and ∂B is its boundary, then by Stokes' theorem and (15)

$$\begin{aligned} \int_{\partial B} \mathbf{v} \cdot dl = \int_B (\nabla \times \mathbf{v}) \cdot \mathbf{n}\, dB = \int_B \mathbf{\Gamma} \cdot \mathbf{n}\, dB = \\ = \int_B (\nabla \times \vec{\mu}) \cdot \mathbf{n}\, dB = \int_{\partial B} \vec{\mu} \cdot dl = const. \end{aligned} \tag{30}$$

Consider the cylindrical surface generated by a set of streamlines leaving the propeller disk at distance r from the axis and the corresponding surface generated by the vortex filaments. At $\alpha = 0°$ the assumption is that these two surfaces remain identical downstream of the disk. Furthermore, at $\alpha = 0°$ the vorticity created by the propeller is independent of θ. Since B is arbitrary in (30) it follows that if $\alpha = 0°$ and the angle between the streamlines and the vortex filaments is constant on each surface, then equation (30) is true also for the stream tubes from the propeller. The circumference of a stream tube is almost constant. Therefore, by (30) our first simplification is

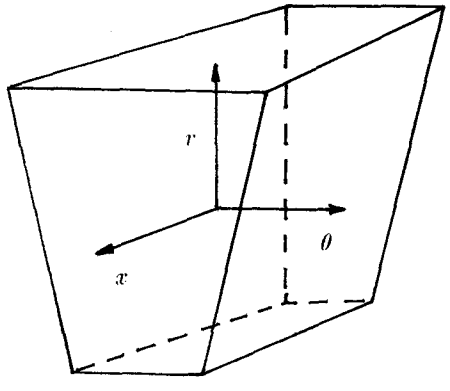

Figure 3: The "field panel" ω_{ijk} and its local coordinate system.

$$\vec{\mu}_{ijk} = \vec{\mu}_{jk},\ i = 1, ..., l, \tag{31}$$

i. e. $\vec{\mu}$ is constant in the stream tubes from the propeller. At $\alpha = 0°$ we have in addition

$$\vec{\mu}_{jk} = \vec{\mu}_k,\ j = 1, ..., m. \tag{32}$$

We now turn to the components of $\vec{\mu}_{jk}$ defined in the local coordinate system in fig. 3

$$\vec{\mu}_{jk} = (\mu_{jkx}, \mu_{jk\theta}, \mu_{jkr})^T.$$

The axes of the local system in each cell are not always completely aligned with the axes of the global cylindrical system. It follows from analogy with wing wakes that μ_{jkr} is small. The first component μ_{jkx} is taken to be constant in ω_{ijk}. For reasons to be explained later we choose a linear variation of $\mu_{jk\theta}$ in the radial direction in ω_{ijk}. Let r_0 and r_1 be the local r coordinate of the bottom and top surface of ω_{ijk} in fig. 3. The widths of these surfaces in the local θ direction are t_0 and t_1, respectively. Then

$$\begin{aligned} \mu_{jk\theta}(r) &= \hat{\mu}_{jk\theta} f(r), \\ f(r) &= 1 + \tfrac{r - r_0}{r_1 - r_0} \left(\tfrac{t_0}{t_1} - 1 \right). \end{aligned} \tag{33}$$

The velocity $\mathbf{v}_{ijk}$ at a point (x, y, z) induced by $\vec{\mu}_{jk}$ in cell ω_{ijk} with surface s_{ijk} is by (14)

$$\begin{aligned} \mathbf{v}_{ijk} = \frac{1}{4\pi} \int_{\omega_{ijk}} \mathbf{\Gamma}_{jk} \times \mathbf{b}\, d\omega \\ -\frac{1}{4\pi} \int_{s_{ijk}} \mathbf{\Gamma}_{sjk} \times \mathbf{b}\, ds. \end{aligned} \tag{34}$$

With definitions analogous to (11) $\mathbf{v}_{ijk}$ can also be written

$$\begin{aligned} \mathbf{v}_{ijk} = \frac{1}{4\pi} \int_{\omega_{ijk}} (\nabla \times \vec{\mu}_{jk}) \times \mathbf{b}\, d\omega \\ -\frac{1}{4\pi} \int_{s_{ijk}} (\mathbf{n} \times \vec{\mu}_{jk}) \times \mathbf{b}\, ds. \end{aligned} \tag{35}$$

Rewrite the first integral in (34) in the same way as (9) is rewritten to (10). It follows from (33) that $\mathbf{\Gamma}_{jk}$ is constant in ω_{ijk}. Thus,

$$\nabla \times \mathbf{\Gamma}_{jk} = 0.$$

We have arrived at a new expression for $\mathbf{v}_{ijk}$ without volume integrals

$$\mathbf{v}_{ijk} = -\frac{1}{4\pi} \int_{s_{ijk}} (\mathbf{n} \times \mathbf{\Gamma}_{jk}/r + \mathbf{\Gamma}_{sjk} \times \mathbf{b})\, ds. \tag{36}$$

The vorticity densities $\mathbf{\Gamma}_{jk}$ and $\mathbf{\Gamma}_{sjk}$ are approximately constant on the surfaces $r \approx$ const. Hence,

$$\mathbf{v}_{ijk} \approx -\frac{1}{4\pi} \left((\mathbf{n} \times \mathbf{\Gamma}_{jk}) \int_{s_{ijk}} 1/r\, ds + \mathbf{\Gamma}_{sjk} \times \int_{s_{ijk}} \mathbf{b}\, ds \right). \tag{37}$$

The volume integral in (35) has been transformed to a surface integral (36),(37). The advantage with surface integrals in (37) is that the same subroutines that were developed for the evaluation of the integrals in the panel program [14] can be reused.

We simplify the representation of the slipstream vorticity further by only taking the contribution from $\mathbf{\Gamma}_{sjk}$ in (37) into consideration. The interpretation of this is that there is a surface distribution of vorticity

$$\mathbf{\Gamma}_{sjk} = \mathbf{n} \times \vec{\mu}_{jk}$$

on each cell face. There is an important computational advantage in using surface vorticity instead of discrete vortex filaments. The velocity is singular at the center of a filament but only the derivative of the velocity is singular when a vortex surface is crossed.

Since we let $\mu_{jkr} = 0$ and $\mu_{jk\theta}$ is constant in the x direction in a stream tube, the singularities on the cell faces $x \approx$ const. will cancel except for the face on the propeller disk. The contribution from the faces with $\theta \approx$ const. will also cancel if the $\vec{\mu}_{jk}$ density is constant in the azimuthal direction and is small if $\alpha \neq 0°$. The induced velocities caused by the vorticity on the faces with $r \approx$ const.

$$\mathbf{\Gamma}_{sjk} = \begin{pmatrix} \Gamma_{sjkx} \\ \Gamma_{sjk\theta} \\ \Gamma_{sjkr} \end{pmatrix} \approx \delta \begin{pmatrix} -\mu_{jk\theta} \\ \mu_{jkx} \\ 0 \end{pmatrix}, \delta = \begin{cases} 1, & r = r_1, \\ -1, & r = r_0, \end{cases}$$

cannot be neglected. At the bottom of the cell in fig. 3 we have

$$\mathbf{\Gamma}_{sjkx} = \hat{\mu}_{jk\theta},$$

and at the top

$$\mathbf{\Gamma}_{sjkx} = -\hat{\mu}_{jk\theta} t_0 / t_1.$$

The choice of $\vec{\mu}_{jk}$ in (33) is motivated by the second vortex theorem in [4] applied to each cell. The amount of vorticity on the bottom face in the x direction

$$\mathbf{\Gamma}_{sjkx} t_0 = \hat{\mu}_{jk\theta} t_0,$$

appears on the top face in the opposite direction

$$\mathbf{\Gamma}_{sjkx} t_1 = -\hat{\mu}_{jk\theta} t_0.$$

Suppose that for each column of cells in a stream tube t_0 and t_1 are constant. Since the vorticity of every cell ω_{ijk} has the above property, then the whole slipstream Ω satisfies the second vortex theorem [4], i. e. a vortex filament never ends in the fluid but closes onto itself, ends at a boundary or goes to infinity.

The system of helical vortices in the slipstream is modeled by a vorticity $\mathbf{\Gamma}_s$ on cylindrical surfaces starting at the propeller disk. The vorticity is composed of ring vortices $\Gamma_{s\theta}$ and axial vorticity Γ_{sx}. It follows from (37) that $\Gamma_{s\theta}$ is responsible for most of the acceleration of $\mathbf{v}$ in the x direction and Γ_{sx} for the swirl in the θ direction.

The vorticity Γ in (22) from the combined momentum-blade element theory in section 2.2 is tranferred to the surface voriticty $\mathbf{\Gamma}_s$ in (37) in the following way. After the simplifications above we are interested in $\mathbf{\Gamma}_{sjk}$ on cylinders starting with a circular section at the propeller and following the streamlines from the disk. Let the direction of the discrete vortex filament be $\mathbf{l}$ from the trailing edge of the propeller blade. The vorticity shed over the distance $r\,d\theta$ is $\Gamma\, r\, d\theta$. The surface corresponding to a vortex of length $d\mathbf{l}$ is $dx\, r\, d\theta$. The angle is ψ between the filament and the disk, cf. (20). Then the surface density $(\Gamma_x, \Gamma_\theta)$ is

$$\begin{aligned} \Gamma\, r\, d\theta\, d\mathbf{l} &= \begin{pmatrix} \Gamma \sin\psi \\ \Gamma \cos\psi \end{pmatrix} r\, d\theta (r\, d\theta / \cos\psi) = \\ &= \begin{pmatrix} \Gamma \tan\psi \\ \Gamma \end{pmatrix} (r\, d\theta)^2 = \\ &= \begin{pmatrix} \Gamma \\ \Gamma / \tan\psi \end{pmatrix} dx\, r\, d\theta = \begin{pmatrix} \Gamma_x \\ \Gamma_\theta \end{pmatrix} dx\, r\, d\theta. \end{aligned}$$

The level of approximation in the panel method is low with flat panels and constant σ_C and μ_C on each panel. Compressibility effects are approximated by the Göthert rule.

3.2 The slipstream geometry.

In the previous subsection the representation of the rotational flow in the discretized slipstream by means of singularity distributions was described. We continue with the generation of the cylinders defining the geometry of the slipstream Ω. Different choices of Ω are possible and this choice is independent of the representation in section 3.1.

The simplest slipstream geometry consists of a number of concentric cylinders with their center on the propeller axis and radius $r_k, k = 0, ..., n$. This is the strategy adopted in many of the papers referred to in section 1. The influence of the slipstream on the nacelle is not very accurate in this approach. A more ambitious model is to let both the nacelle and the wing participate in the shaping of the cylinders. This will probably be a rather complicated process, see [7]. We have chosen a middle way between these two extremes by letting the propeller disk, the nacelle surface and a trailing sting determine the geometry of the slipstream. The sting is added to the base of the nacelle to model the flow better in that region and to simulate windtunnel conditions.

The cylinder surfaces in the slipstream geometry are the stream surfaces emanating from circles on the propller disk. The streamlines defining the stream surfaces are calculated by the panel method [14]. If the velocity component $\mathbf{v}_1$ from the slipstream is small in comparison to $\mathbf{v}_2$ then the generated stream surfaces are fairly representative of the the true stream surfaces in Ω. If the slipstream velocities are stronger then the deviations are larger, e. g. in the radial direction where the contraction of the slipstream is ignored. Note that if $\alpha = 0°$ then there is no need to follow the θ or swirl component of the streamlines, since $\vec{\mu}_{jk}$ and $\mathbf{\Gamma}_{jk}$ are constant for $j = 1, ..., m$.

The procedure to obtain the streamlines is as follows. Panel the propeller disk with m panels in the azimuthal direction and n in the radial direction. Each panel corner $\mathbf{r}^0_{jk}$ is the initial point of a streamline. At a point $\mathbf{r}^N_{jk}$ the velocity $\mathbf{v}^N_{jk}$ caused by the freestream and the simplified configuration is calculated by the panel method [14]. A suitable time-step Δt_N is chosen.Then the iteration from $N = 0$

$$\mathbf{r}_{jk}^{N+1} = \mathbf{r}_{jk}^{N} + \Delta t_N \mathbf{v}_{jk}^{N},\ j = 1,...,m, k = 1,...,n,$$

is continued until x_{end} is passed.

The slipstream cylinders are partitioned into panels. The velocity $\mathbf{v}_1$ due to the slipstream is computed at the midpoint of every cell ω_{ijk}. This velocity is the sum of the contributions from the singularity densities in all the cells in Ω. By linear interpolation between the velocities $\mathbf{v}_{1ijk}$ at the midpoints, $\mathbf{v}_1$ at an arbitrary point, e. g. the panel midpoints of the configuration surface, can be computed.

4 Computational results and comparisons.

In the low speed windtunnel experiments in [21] and [22] two configurations with a wing are tested. One model has an axisymmetric nacelle and a straight wing with symmetric profile mounted symmetrically on the nacelle. The other model has the same wing but the nacelle is non-axisymmetric with the propeller axis located over the wing. A detailed description of the geometry of the models is found in [21]. The pressures and velocities around these configurations computed by CRAY X-MP are compared to the measured values in this section.

The axisymmetric nacelle and its wing are paneled in fig. 4. The propeller has four blades and its position and size are depicted in fig. 8. The wing profile is $NACA\ 63_{(10)}A-012$. The discontinuity in the static pressure at the propeller disk is determined by the condition on the pressure in the fully contracted slipstream, see section 2.3.

The discretization of the geometry of the non-axisymmetric nacelle and its wing is found in fig. 5. The geometry of the windtunnel model is modified in the computations for the following reason. The slipstream model in section 3.2 assumes that no streamlines from the propeller disk

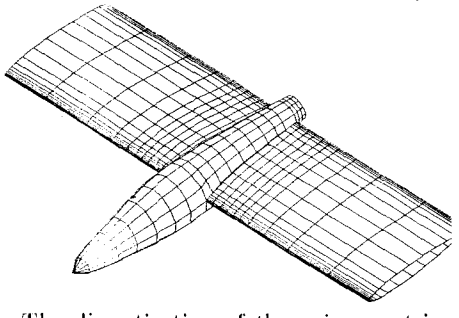

Figure 4: The discretization of the axisymmetric nacelle with wing.

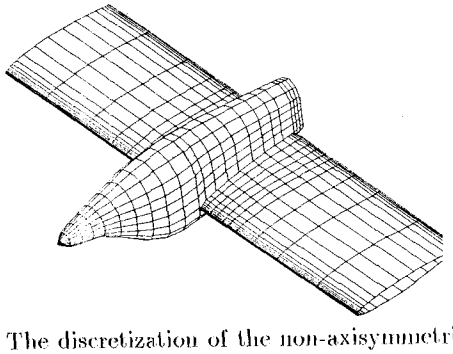

Figure 5: The discretization of the non-axisymmetric nacelle with wing.

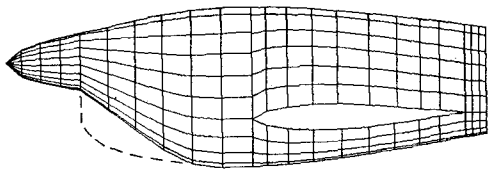

Figure 6: A side view of the modified geometry in the computations with the non-axisymmetric nacelle with wing. The original geometry is indicated by dashed lines.

hit the nacelle surface. This does not seem to be the case with the original geometry. The frontal part of the nacelle is therefore changed to suit the computations better, see fig. 6. The assumption is that the flow over the wing is not altered very much by this change of geometry. The propeller and wing profile are the same as above.

The cylindrical surfaces representing the slipstream geometry are generated around the nacelles without wings, cf. section 3.2. The cross sections of the cylinders in the $\theta - r$ plane at $\alpha = 0°$ at a few x stations are shown in fig. 7 for the axisymmetric and non-axisymmetric nacelle.

The Mach number in the experiments and the computations is 0.15. The propeller thrust coefficient C_T and the advance ratio J are defined by

$$C_T = T/(\rho_\infty N^2 D^4),\ J = v_\infty/(ND),$$

where N is the rotational speed of the propeller and D is the diameter. The value of C_T is about 0.22 and J is 0.70.

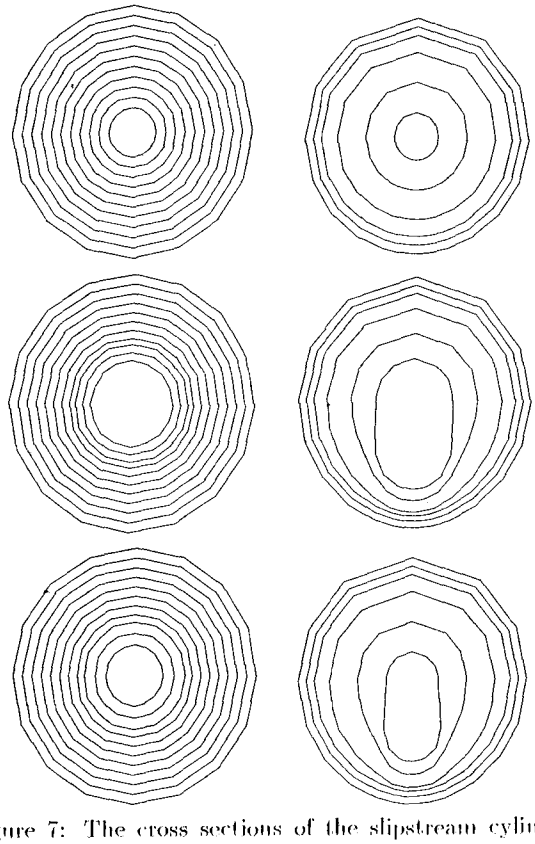

Figure 7: The cross sections of the slipstream cylinders around the axisymmetric (left) and the non-axisymmetric (right) nacelle. The sections are from right behind the propeller (top), the middle of the nacelle (middle) and the end of the nacelle (bottom).

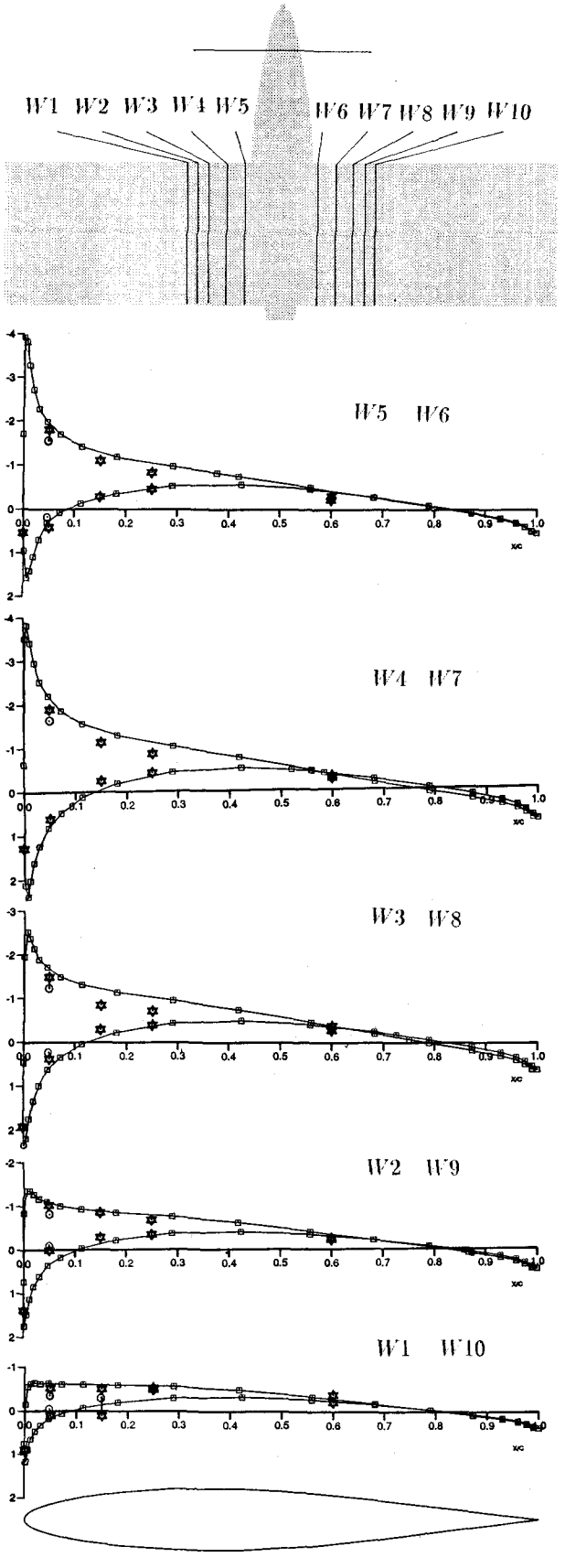

Figure 8: The c_p values at $\alpha = 0°$ at different sections on the wing with the axisymmetric nacelle. The computed values are marked by □ and the experimental values by ⋆ and ⊙.

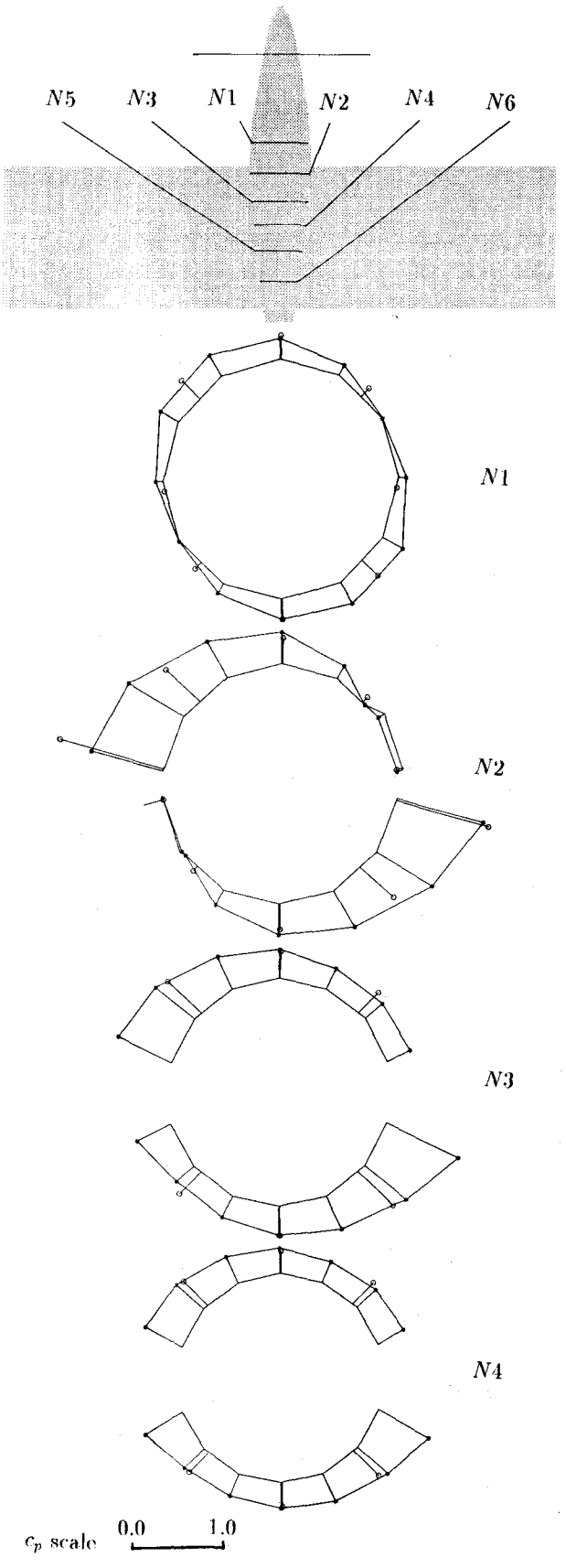

Figure 9: The c_p values at $\alpha = 0°$ at different sections on the axisymmetric nacelle. The computed values are marked by ∗ and the experimental values by ⊙.

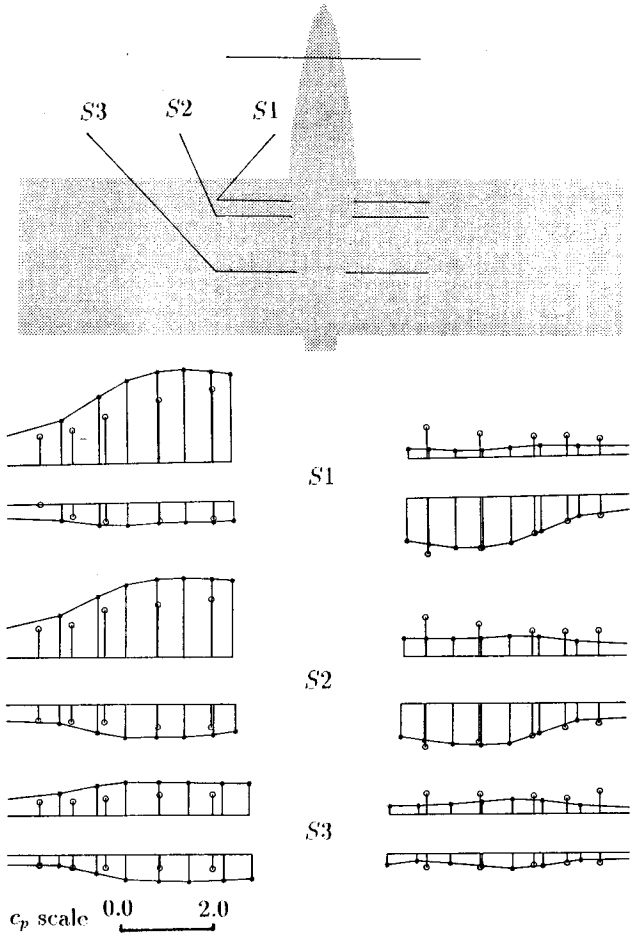

Figure 10: The c_p values at $\alpha = 0°$ at different sections on the wing with the non-axisymmetric nacelle. The computed values are marked by $*$ and the experimental values by ⊙.

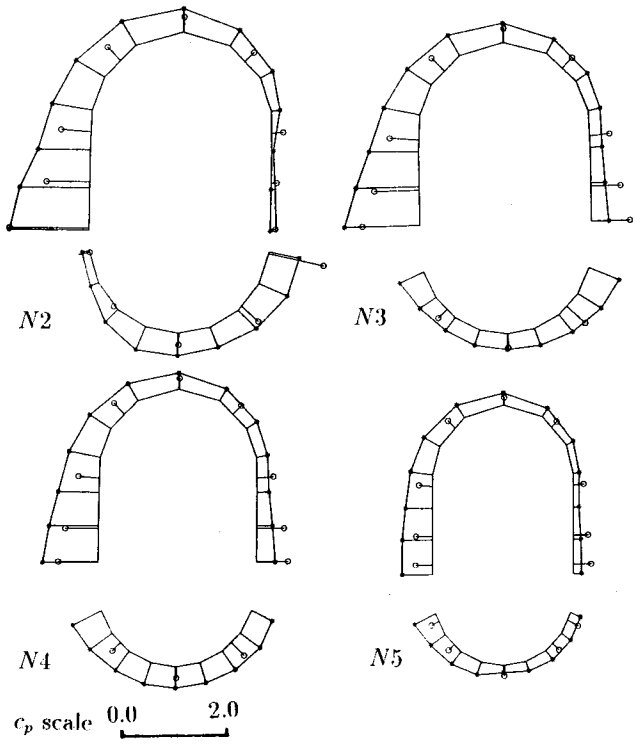

Figure 11: The c_p values at $\alpha = 0°$ at different sections defined in fig. 9 on the non-axisymmetric nacelle. The computed values are marked by $*$ and the experimental values by ⊙.

In the first example the pressures on the axisymmetric nacelle and its wing are computed and compared to the experimental values. The propeller rotates in the negative θ direction. At $\alpha = 0°$ the flow field is anti-symmetric around the propeller axis. The flow above the starboard wing is identical to the flow below the port wing and vice versa. This anti-symmetry is reproduced very well in the computations. The anti-symmetry is not perfect in the windtunnel data. In fig. 8 the c_p values on the port wing are compared. If the two measured values from the starboard (⊙) and port ($\star$) wing that should be equal are a little apart, then both values are plotted and combined by a line. The nacelle pressures are displayed in fig. 9 looking upstream. The length of an arrow is proportional to the

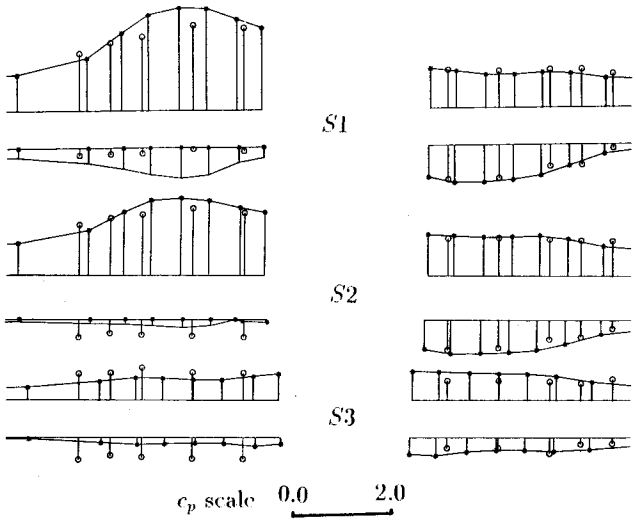

Figure 12: The c_p values at $\alpha = 5°$ at different sections defined in fig. 10 on the wing with the axisymmetric nacelle. The computed values are marked by $*$ and the experimental values by ⊙.

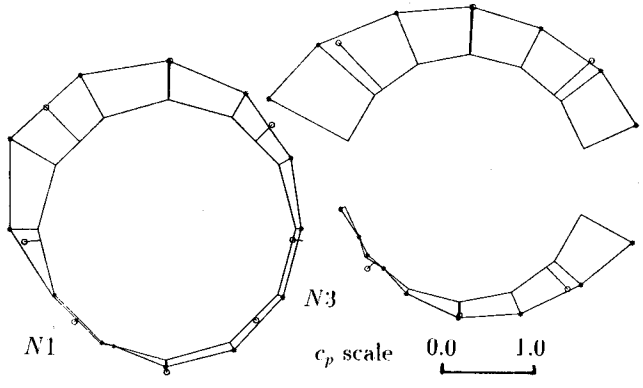

Figure 13: The c_p values at $\alpha = 5°$ at two sections defined in fig. 9 on the axisymmetric nacelle. The computed values are marked by $*$ and the experimental values by ⊙.

c_p value at its foot. The markers on the arrows are placed at the nacelle surface if c_p is positive and away from the surface if c_p is negative. The agreement between calculated and experimental data is good in this case.

The c_p values for the non-axisymmetric nacelle and the wing at $\alpha = 0°$ are plotted and compared in figs. 10 and 11. The port side is to the left and the starboard side is to the right in the c_p plots. The extension of these plots in the r direction is indicated in the configuration overview at the top. The effect of the slipstream is overestimated in the computations in comparison to the experiments.

The results at $\alpha = 5°$ for the axisymmetric configuration is shown in figs. 12 and 13. We have chosen the same slipstream geometry as in the case $\alpha = 0°$, but the momentum-blade element theory is modified to handle an α different from 0. Also here the effect of the slipstream is greater in the calculated values than in the measured values.

The velocities in the flow field outside the nacelles over the wing are compared in fig. 14 at $\alpha = 0°$. The velocities around the axisymmetric nacelle are anti-symmetric such that $\mathbf{v}$ at $\theta = 45°$ is equal to $\mathbf{v}$ at $\theta = 315°$ and so on. The numerical solution has this property but there are small deviations from anti-symmetry in the experimental data. The velocities are proportional to the abscissa in fig. 14. Note that the abscissa scales are diffrent in the v_x and the v_θ plots. The ordinate is the distance from the propeller axis divided by the propeller radius. The velocity is almost discontinuous at the outer boundary of the slipstream. The difference between the calculated and measured velocities are of the same order in the x and θ directions.

5 Conclusions and discussion.

A *computational model of the slipstream behind a propeller* has been developed and implemented in an existing panel program environment. The vortical flow in the slipstream is represented by a surface vorticity distribution $\mathbf{\Gamma}_S$ on cylindrical surfaces approximating the internal structure of the slipstream. The vorticity $\mathbf{\Gamma}_S$ is computed by a combined momentum-blade element theory. The calculations are compared to windtunnel results for two configurations: an axisymmetric nacelle with a wing and a non-axisymmetric nacelle with a wing. In the first case at $\alpha = 0°$ the computed pressures and velocities agree well with the experiments. The influence of the slipstream on the c_p values on the surfaces of the non-axisymmetric configuration is greater in the computations in comparison with the measurements. The results for the axisymmetric nacelle at $\alpha = 5°$ are good on the nacelle and of the same quality on the wing as in the non-axisymmetric case.

There are several possible explanations to the discrepancies between the computed and the experimental data. The following assumptions and approximations may be major or minor sources of error in the computational model.

- The geometry of the slipstream is not dependent on flow generated by the propeller. Hence, there is no contraction of the slipstream geometry caused by the propeller as predicted by classical propeller theory. By computing the outer boundary and the inner structure of the slipstream in an iterative fashion the contraction of the slipstream could be modeled, see e. g. [17].

- It is clearly visible in windtunnel experiments that the wings change the shape of the slipstream geometry. The symmetry between the port and starboard sides of the geometry is lost. The inclusion of such a possibility in the present approach seems very complicated.

- The combined momentum-blade element theory of the propeller behavior is simple. Nevertheless it seems to work at least for small Mach numbers and $\alpha = 0°$. More advanced theory is possible which can be complemented by windtunnel data, see [13].

- One can show that the computations of c_p is sensitive to errors in the slipstream velocity $\mathbf{v}_2$. The c_p value is calculated by the usual formula based on Bernoulli's equation and then corrected by the jump at the disk. Often two numbers of similar size are subtracted to obtain c_p leading to cancellation of terms. The relative error in the result is much greater than the relative errors in the two terms.

- When $\alpha \neq 0°$ then $\mathbf{\Gamma}_S$ is no longer constant in the θ direction. The variable $\mathbf{\Gamma}_S$ is transported downstream in a helical manner. This effect can be included in the present code in a relatively simple way.

- The model geometry in the windtunnel experiments is not exactly the same as the geometry in the computations. The necessary change of the non-axisymmetric nacelle may be important to the flow over the wing.

- There are a number of numerical approximations made in the implementation of the slipstream model. As an example we mention the conservation of the vorticity density which is only approximate in the computations.

- The geometry of the nacelle does not affect the performance of the propeller in the blade element theory.

Finally, we remark that there are errors also in the windtunnel experiments. The deviation from anti-symmetry for the axisymmetric nacelle $\alpha = 0°$ provides a measure of that uncertainty.

References

[1] A. S. Aljabri, The prediction of propeller/wing interaction effects, ICAS paper ICAS-82-4.4.5, 1982.

[2] A. S. Aljabri, Aerodynamic design of propfan powered transports, AIAA paper AIAA-83-1213, 1983.

[3] A. Amendola, R. Tognaccini, J. W. Boerstoel, A. Kassies, Validation of a multi-block Euler flow solver with propeller-slipstream flows, in *Validation of Computational Fluid Dynamics*, AGARD Conference Proceedings, Vol. 2, No 437, Neuilly-sur-Seine, France,

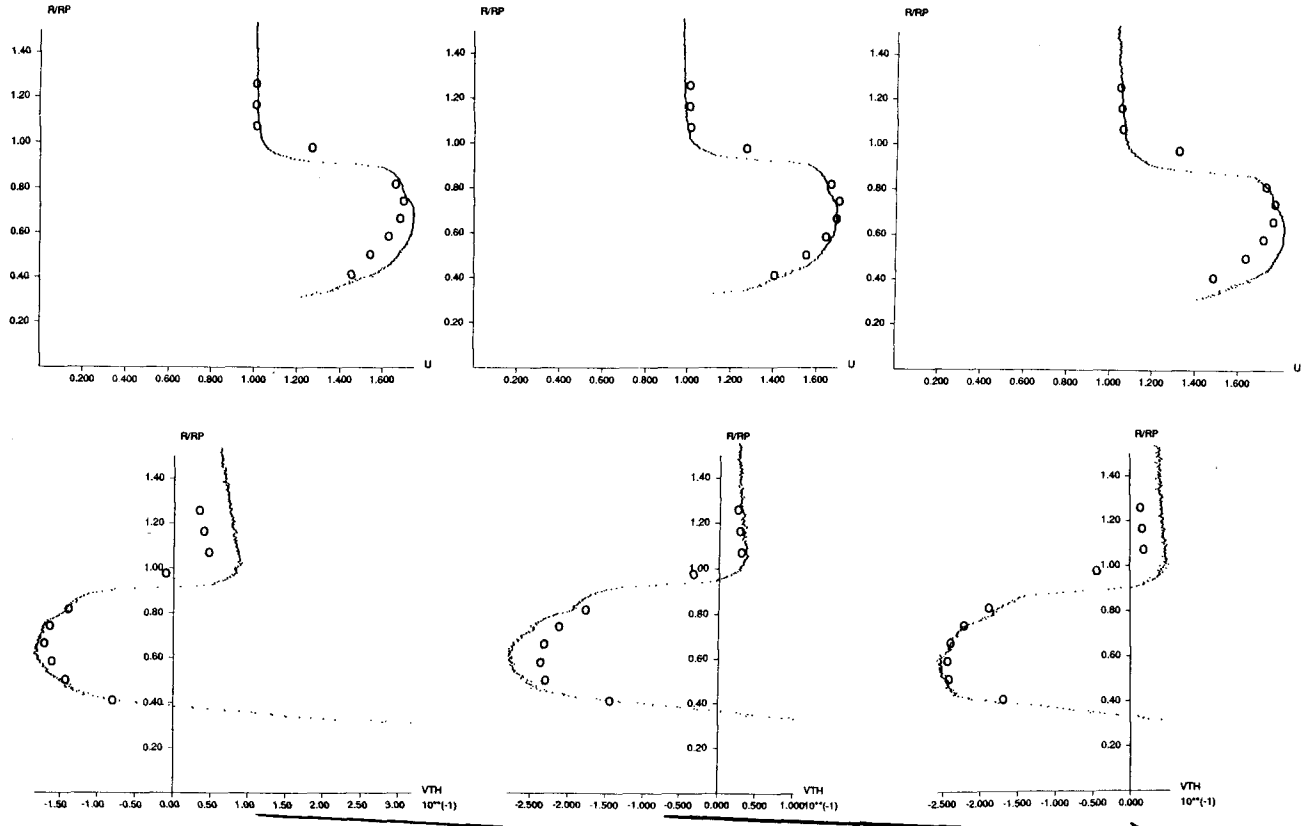

Figure 14: The velocities at $\alpha = 0°$ in the flow field around the axisymmetric nacelle with wing (top) and the non-axisymmetric nacelle with wing (bottom). The flow field at $N3$ is shown at angles as depicted in the frontal view of the configurations. The speed in the x direction is plotted in the top row for the axisymmetric case and to the left for the non-axisymmetric case. The θ speed is plotted in the bottom row and to the right in the respective case. The computed values are marked by ○ and the experimental values by ·.

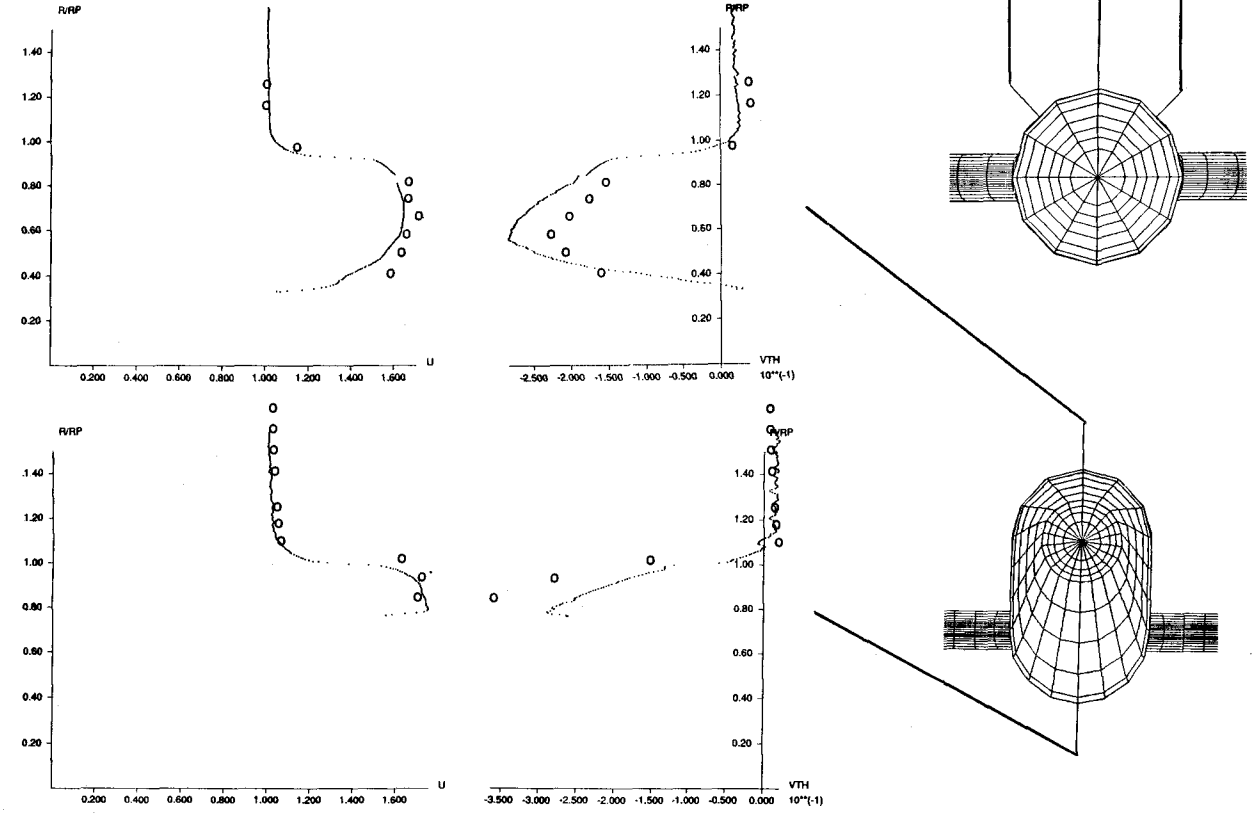

1988.

[4] H. Ashley, M. Landahl, *Aerodynamics of Wings and Bodies*, Addison-Wesley, Reading, MA, 1965.

[5] C. W. Boppe, B. S. Rosen, Computation of prop-fan engine installation aerodynamics, *J. Aircraft*, 23, 1986, pp 299-305.

[6] R. L. Carmichael, L. L. Erickson, PANAIR - A higher order panel method for predicting subsonic or supersonic linear potential flows about arbitrary configurations, AIAA paper AIAA-81-1255, 1981.

[7] D. R. Clark, The use of panel methods in the calculation of the flows around general configurations including the coupled effects of rotors and propellers, in *Proceedings of Computational Fluid Dynamics in Aerospace Design Workshop*, University of Tennessee Space Institute, Tullahoma, TN, 1985, pp 11.0-11.34.

[8] R. W. Clark, W. O. Valarezo, Subsonic calculation of propeller/wing interference, AIAA paper AIAA-90-0031, 1990.

[9] J. L. Hess, W. O. Valarezo, Calculation of steady flow about propellers using a surface panel method, *J. Propulsion and Power*, 1, 1985, pp 470-476.

[10] H. Glauert, Airplane propellers, in *Aerodynamic Theory*, Vol. IV, ed. W. F. Durand, Springer, Berlin, 1935.

[11] H. W. M. Hoeijmakers, Panel methods in aerodynamics; Some highlights, in *Panel Methods in Fluid Mechanics with Emphasis on Aerodynamics*, eds. J. Ballmann, R. Eppler, W. Hackbusch, Notes on Numerical Fluid Mechanics, Vol. 21, Vieweg, Braunschweig, 1988, pp 1-34.

[12] C. Kirrmann, A. Rousseau, M. Yermia, Calcul du soufle moyen d'une hélice et de son influence sur les performances d'un avion, *L'Aéronautique et L'Astronautique*, No 101, 1984, pp 45-61.

[13] C. N. H. Lock, R. C. Pankhurst, J. F. C. Conn, Strip theory method of calculation for airscrews on high-speed aeroplanes, R. & M. No 2035, Aeronautical Research Council Technical Report, His Majesty's Stationery Office, London, 1945.

[14] P. Lötstedt, Evaluation of a higher order panel program for subsonic flow, in *Panel Methods in Fluid Mechanics with Emphasis on Aerodynamics*, eds. J. Ballmann, R. Eppler, W. Hackbusch, Notes on Numerical Fluid Mechanics, Vol. 21, Vieweg, Braunschweig, 1988, pp 147-155.

[15] B. Maskew, Prediction of subsonic aerodynamic characteristics: A case for low-order panel methods, *J. Aircraft*, 19, 1982, pp 157-163.

[16] B. W. McCormick, Jr, *Aerodynamics of V/STOL Flight*, Academic Press, New York, 1967.

[17] M. P. Metcalfe, On the modelling of a fully-relaxed propeller slipstream, AIAA paper AIAA-85-1262, 1985.

[18] J. P. Narain, A transonic analysis of propfan slipstream effect on a supercritical wing, AIAA paper AIAA-83-0186, 1983.

[19] S. S. Samant, N. J. Yu, Flow prediction for propfan engine installation effects on transport aircraft at transonic speeds, NASA Contractor Report 3954, 1986.

[20] S. S. Samant, N. J. Yu, P. E. Rubbert, Transonic flow simulation of prop-fan configurations, AIAA paper AIAA-83-0187, 1983.

[21] I. Samuelsson, Low speed wind tunnel investigation of propeller slipstream aerodynamic effects on different nacelle/wing combinations, ICAS paper ICAS-88-4.11.1, 1988.

[22] I. Samuelsson, Experimental investigation of low speed model propeller slipstream aerodynamic characteristics including flow field surveys and nacelle/wing static pressure measurements, ICAS paper ICAS-90-3.1.3, 1990.

[23] W. O. Valarezo, Calculation of isolated and installed multiple rotor flows using a surface panel method, AIAA paper AIAA-89-2211, 1989.

[24] D. L. Whitfield, A. Jameson, Three-dimensional Euler equation simulation of propeller-wing interaction in transonic flow, AIAA paper AIAA-83-0236, 1983.